Journal of Power Sources 191 (2009) 582–590

Contents lists available at ScienceDirect

Journal of Power Sources

journal homepage: www.elsevier.com/locate/jpowsour

Characterisation of charge and discharge behaviour of lithium ion batteries with olivine based cathode active material

Michael A. Roscher[a,*], Jens Vetter[b], Dirk Uwe Sauer[a]

[a] RWTH Aachen University, Electrochemical Energy Conversion and Storage Systems Group, Institute for Power Electronics and Electrical Drives (ISEA), 52066 Aachen, Germany
[b] BMW Group, 80788 München, Germany

ARTICLE INFO

Article history:
Received 1 December 2008
Accepted 8 February 2009
Available online 20 February 2009

Keywords:
Li-ion battery
Olivine cathode
Phase transition
Power capability

ABSTRACT

This paper gives insight to the physical processes taking part during the two-phase transition in lithium intercalation compounds. The behaviour of olivine based electrodes is in the special focus of this work. These electrodes exhibit phase juxtaposition within the electrode particles over a wide state of charge (SOC) range. Measurements were made to explore effects related to the formation of distinct phase sequences within the particles. Asymmetric charge characteristics, a load history dependency of the internal resistance and a voltage effect related to the disappearance of certain phase regions (the later on called vanishing phase effect) were identified. Moreover, these measurements give evidence to the existence of stable phase regions inside the electrode active material. An intuitive model is given to visualize the phase regions within spherical olivine particles. Therefore an analytical approach is developed in order to take the geometry of the particles, the ion permeability as well as the size distribution of the particles in consideration. According to the developed approach and the obtained measurement results, an enhanced cell equivalent electrical circuit is evaluated, considering phase shell development effects.

1. Introduction

In the recent years, lithium-ion batteries (Li-ion) have replaced the predominant nickel metal hydride batteries (NiMH) in most portable consumer electronics because of their high energy density and power density. These advantages spurred further researches and developments with emphasis on new chemistries and manufacturing methods.

In 1997, Goodenough et al. introduced the lithium iron phosphate ($LiFePO_4$) as promising cathode material for Li-ion batteries [1,2]. In contrast to more prevalent layered and spinel type cathode materials $LiFePO_4$ has an olivine structure. It has a density of $3.6\,g\,cm^{-3}$ and a theoretical capacity of $170\,mAh\,g^{-1}$ with an electrochemical potential of 3.5 V against Li/Li^+ [3]. Even though $LiFePO_4$ based systems have a reduced operating voltage in comparison to usual LiM_xO_{2x} cathode materials, it shows a number of advantages in use. $LiFePO_4$ based systems are nontoxic, behave intrinsic safe, have low metal costs and show good cycle life performance.

The performance of the first $LiFePO_4$ cathodes was restricted by the poor electric conductivity ($10^{-9}\,S\,cm^{-1}$) of the active material. Recently, several innovations made it possible to enhance the conductivity of the cathodes significantly by fabricating cathodes with very small and carbon coated particles [4–6]. Doping the bulk material with transition metal atoms (e.g. Mg, Ti, Nb, Zr, Al, W [3,7]) led to a further improvement of cathodes performance. These cathodes have volumetric energy densities of approximately $2000\,Wh\,l^{-1}$ (higher than $LiMn_2O_4$), respectively, a specific energy of $540\,Wh\,kg^{-1}$ (higher than $LiCoO_2$) [4].

A special feature of $LiFePO_4$ based electrodes is the constant operating voltage which is nearly independent from the state of charge (SOC). The open circuit voltage (OCV) changes under 100 mV in a range of 20–80% of SOC. In the boundary regions the gradient of OCV increases. The mentioned advantages in use are counteracted by some arising difficulties in estimating the SOC from the voltage at the batteries terminals, due to the slight gradient in the SOC/OCV characteristic.

The constant electrode voltage of olivine Li_xFePO_4 with varying Li content x has its origin in a two-phase transition taking place in the active material. Thus, lithium intercalation in $LiFePO_4$ electrodes is in the focus of the following sections. Models to describe and quantify effects caused by the two-phase behaviour will be given. Moreover, the vanishing phase effect typical for two-phase systems will be introduced and elucidated. Finally the established models will be validated on the basis of measurements with olivine–graphite cells.

* Corresponding author. Tel.: +49 89 38211380; fax: +49 89 3827011380.
E-mail address: michael.roscher@rwth-aachen.de (M.A. Roscher).

0378-7753/$ – see front matter © 2009 Elsevier B.V. All rights reserved.
doi:10.1016/j.jpowsour.2009.02.024

2. Review to first order phase transition intercalation compounds

The occurrence of two-phase transition behaviour has already been published (e.g. [8,9]) as mentioned above. This effect is characteristic not only for the intercalation of Li ions in lattices of various materials. Subramanian et al. report this effect also to take place during the admission of hydrogen molecules into electrodes of NiMH cells [10].

The two-phase state of lithium intercalation compounds can be generally paraphrased by the coexistence of two different substances in a solid state which is formed out of an original homogenous material. In this case the two substances vary in the distinct Li concentrations (c_{Li}). Barriers exist between the substances forming phase regions inside e.g. the active particles of an electrode. During the admission or extraction of lithium the barriers move within the particles with the distinct Li concentration remaining constant. Through a first order transition one substance is transformed to the particular counterpart at the moving barrier. During the two-phase transition the electrode potential remains constant due to the constant c_{Li} inside the phase regions. Thus, two-phase transition materials show characteristic minima of the differential electrode potential (∂OCV/∂SOC) and maxima of the differential capacity (∂C/∂OCV). These are identifiable as typical plateaus in the cell voltage during constant current charge or discharge.

Levi et al. relate the existence of the two-phase transition behaviour to intensive attractions between the Li (guest) and the host lattice. These attractions avoid the homogenous alloy composition in some defined SOC intervals. Certain Li concentrations are energetic favourable to the host lattice (minima of the free energy) [11,12]. Additional energy has to be applied to the lattice in order to overcome the energy barriers in-between the minima, i.e. via applying an overvoltage to the certain cell [9]. The number of energy minima and maxima is depending on the specific properties of the host lattice, so more than one OCV plateau is possible within the whole SOC range. The Frumkin isotherm theory gives a feasible model and an analytic approach to describe and quantify the guest to host attraction as a function of c_{Li} and the temperature [13]. Meethong et al. and Levi et al. are additionally reporting the particle size or the the layer thickness of an electrode to be a factor influencing the occurence of the two-phase transition [14,15]. In their opinion small particles/thin active layers tend to undergo a homogenous solid state intercalation process at elevated temperatures (60 °C and higher).

Cathode materials such as $LiCoO_2$, $LiNiO_2$ and even $LiFePO_4$ and graphite as the widest spread commercial anode material for Li-ion batteries are typical substances exhibiting two-phase transition intercalation.

The two-phase transition caused voltage plateau of $LiCoO_2$ is associated to an electrode potential of 3.95 V (Li/Li^+) [13]. In regions of higher and lower electric potential these electrodes behave like a normal diffusion intercalation compounds. The electrical characteristic is determined by the dynamics of the diffusion processes only.

$LiNiO_2$ based electrodes are showing three two-phase transitions within the possible c_{Li} range. The respective voltage plateaus can be found at approximately 3.57 V, 3.66 V and 4.04 V (Li/Li^+). Furthermore, there are two other peaks in ∂C/∂OCV at voltages of 3.76 V and 3.93 V identifiable. However, these peaks are related to restructuring processes inside the crystal lattice, not to two-phase regions [13]. Though, $LiCoO_2$ as well as $LiNiO_2$ shows two-phase transition behaviour, $LiCo_{0.2}Ni_{0.8}O_2$ composite electrodes do not [13].

For Li_xFePO_4 one region with typical two-phase behaviour is known in the range $0 < x < 1$. The voltage of the OCV plateau resides on a level of approximately 3.5 V (Li/Li^+). In the literature there is more than one information given according to the width of the sector (SOC = 0–100%) in which the first order transition is taking place. Gabersek et al. report the two-phase transition to appear between 11% and 95% SOC (correlating to $0.05 < x < 0.89$ in Li_xFePO_4) [8]. Srinivasan and Newman relate the two-phase region to 4.75–98% SOC (correlating to $0.02 < x < 0.9525$ in Li_xFePO_4), in contrast [16]. In spite of this slight different data mentioned, it can be assumed that the intercalation process of $LiFePO_4$ based cells is mainly characterised by the two-phase transition behaviour.

In graphite, the most common anode material of nowadays Li-ion cells, six different concentration states are known with two-phase transition regions situated in-between.

In the following section the Li intercalation in $FePO_4$ is described more in details in order to give a comprehensive overview to the dedicated mechanisms taking place.

3. Modelling of two-phase transition of $LiFePO_4$ electrodes

With the shrinking core theory (Subramanian et al. [10]) it is possible to develop an intuitive approach for the microscopic processes during two-phase transition of intercalation compounds. It is assumed that electrodes are consisting of spherical particles covered with a substance having an ideal conductivity. Furthermore, the particles are assumed to be homogenous in terms of structural formation and to have isotropic electric conductivity in both, the complete charged and complete discharged state, even though, the redox reactions ($Li^+ + e^- \rightarrow Li$) at the particles surface is assumed to be ideal. Thus, the finite conductivity of the electrode active material is the unique limiting factor to the movement of lithium atoms.

The spatial and temporal sequence of the phase regions of a composite particle during lithium intercalation is depicted in Fig. 1a. The lithium content increases while discharging the electrode (Li insertion), determined by diffusion dynamics. After reaching the specific concentration limit ($c_{Li} = c_{max}$) the two-phase transition takes place. A phase shell with $c_{Li} > c_{max}$ develops around a core. The Li concentration within the core remains at c_{max} (Li-poor spherical region).

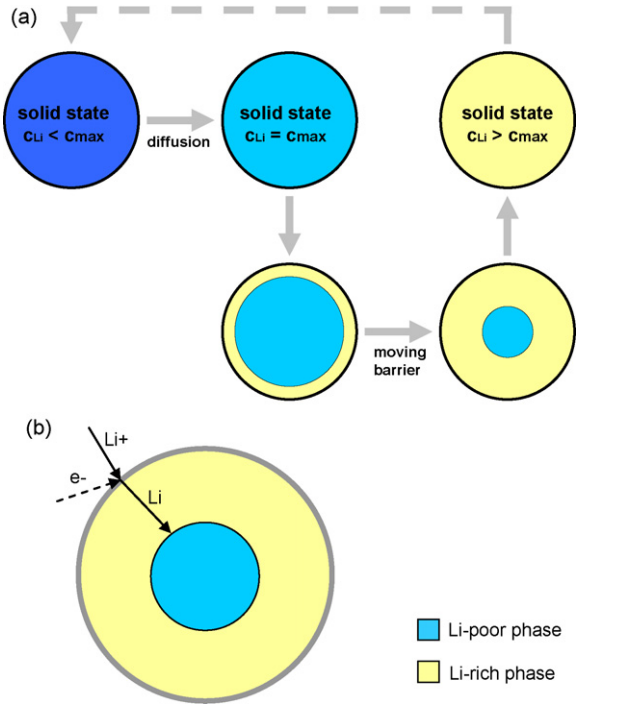

Fig. 1. Phase separation during two-phase transition Li intercalation process (a) and path of the charge carriers the Li atoms during intercalation (b).

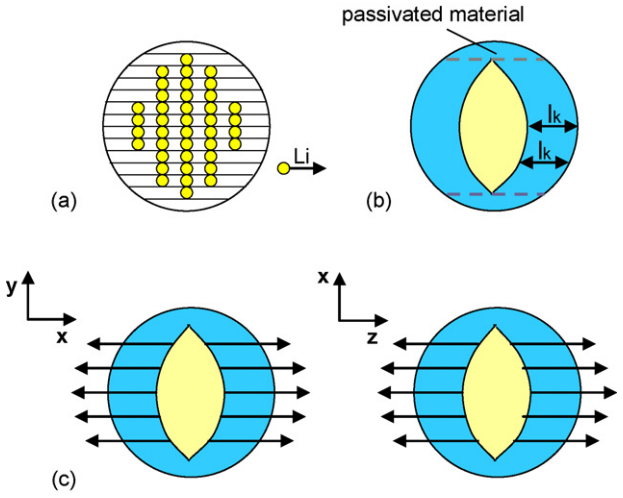

Fig. 2. The 1D channels existing in $LiFePO_4$ illustrated (a), uniform growth of the shell section and passivated belt region (b), lentoid core during two-phase transition (c).

The Li concentration of the shell region is higher than c_{max} but remains constant also (Li-rich region). Additional Li is embedded to the outer shell of the spherical particle. The barrier between the regions shifts toward the centre of the particle. After the core has vanished completely the particles material is homogenous again. Subsequently the next two-phase transition follows or the intercalation continues undergoing a solid state reaction.

Fig. 1b illustrates a possible path the Li might migrate inside the bulk material. As the shell region grows the lithium has to cover longer distances to become intercalated into the lattice at the region barrier.

In case of alternating the load current (discharge → charge) during the two-phase state an additional Li-poor shell emerges at the surface of the particle. The growth of new shells always starts at the particle surface with a new region barrier moving toward the centre. Thus, it is possible to form particles structures with any number of alternating layers.

For real electrodes some of the assumptions met above are not correct. One is the not ideal surrounding of particles with an ideal conductive phase, depending on the geometry and the content of conductive additives [17]. Another one is the matter of having isotropic conductivity which is not given for most electrode materials, due to their structural properties. The layered structure of graphite only permits the movement of Li in two of the three spatial directions *x*, *y*, *z*. Moreover, in the olivine structured $LiFePO_4$ the Li atoms are able to move in just one of the three possible spatial directions. The atoms migrate through 1D channels within the electrode material [18]. This specific property causes the formation of lentoid cores during intercalation of spherical particles, assuming the electrode to contain monocrystalline particles only (Fig. 2c). Fig. 2a schematically illustrates the growing shell where the extraction of Li ions occurs. The length l_k of the Li-poor sections of the 1D channels increases uniformly (Fig. 2b). The Li atoms migrate from the Li-rich core to the particles surface with respect to the assumption met earlier in this chapter. The described process continues until every channel is in the Li-poor state.

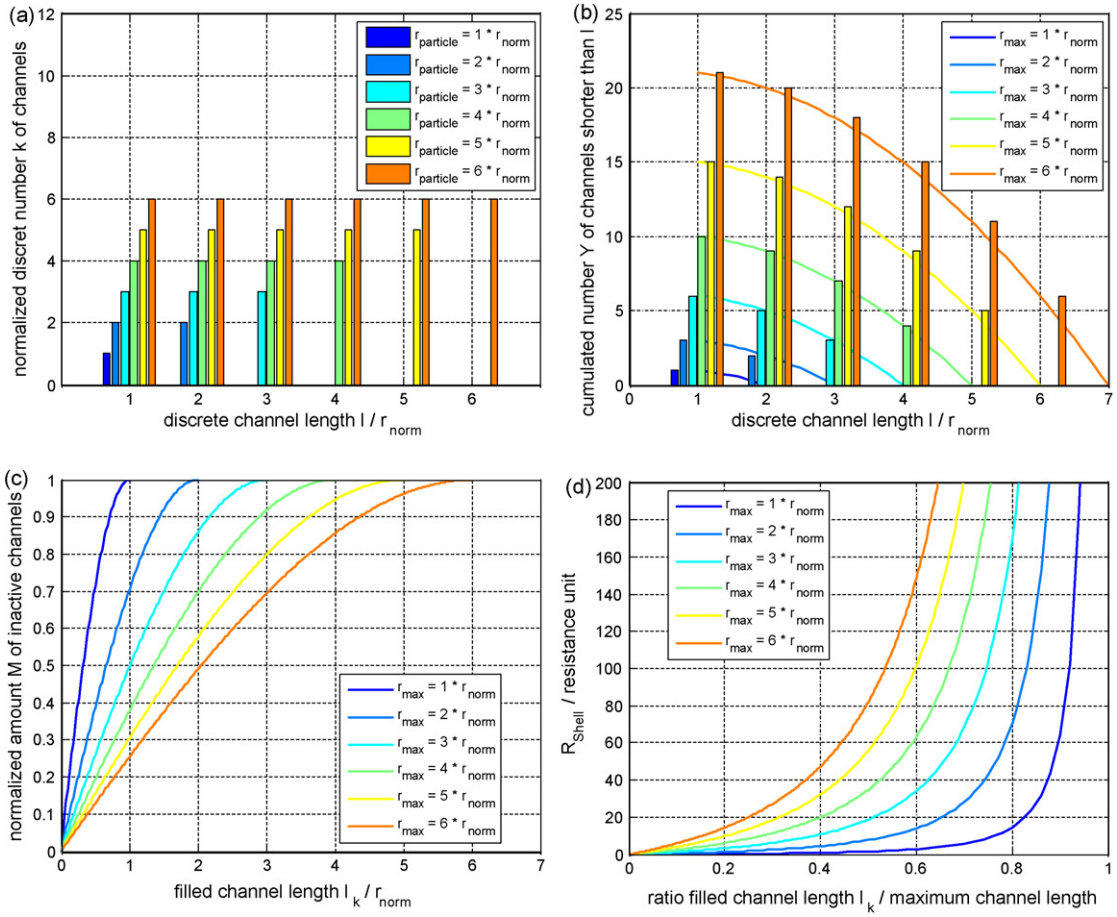

Fig. 3. Illustration of the distribution of discrete channel lengths within particles having different sizes (a), amount of channels having discrete lengths within an electrode with uniformly distributed particle sizes (b), content of passivated channels during two-phase transition (c) and shell phase resistance development for different size distributions (d).

Depending on the specific geometry of the particles, channels with differing effective lengths exist within a certain particle and within a certain $LiFePO_4$ based electrode. It becomes possible that some of the channels are completely Li depleted while other ones are still partial Li-rich. The depleted channels are inactive for the transport of the lithium. They form a passivated belt enclosing the still active core. The width and thickness of this belt increases with ongoing Li extraction (illustrated in Fig. 3b). Concerning to the particles shape, the particles contacting and the dynamics of the surface reaction, it is possible to obtain shell regions and core regions having various shapes [12,18].

The hindered Li movement causes overvoltage effects during load of the cathodes due to apparent diffusive voltage drops. To model these voltage drops an ohmic resistance of the shell regions can be assumed, contributing to the internal cell resistance. Hence, the resistance of each channel as well as the resistance of the whole shell region can generally be calculated with Eq. (1).

$$R_{\text{channel}} = \frac{l_k}{k} \rightarrow R_{\text{Shell}} = \frac{1}{n}\frac{l_k}{k} \tag{1}$$

In this equation l_k represents the present length of the outer section of the still active channels and k (S m) is related to the specific Li conductivity of just one 1D channel. The factor n comprises the number of still active channels. Thus, the absolute length of each channel is not crucial but influences n, due to the particle shape. In case of electrodes containing spherical particles with uniformly size distribution, an analytical approach for the n and R_{Shell} of a real electrode can be given as follows.

Each 1D channel is able to assimilate a certain amount of Li atoms, thus discrete utilisable channel lengths l (a multiple of the scale factor r_{norm}, with channels of the length r_{norm} are able to contain one Li atom) can be assumed. For each spherical particle (radius r_{particle}) a distinct channel length distribution ($g_{(l)}$) can be calculated with Eq. (2), considering r_{particle} and the cross-section area (A_{channel}) of just one channel, due to the uniformly distributed lengths of channels within spherical particles. In Fig. 3a the discrete length distributions are given for six different particle sizes (discrete channel length distribution $l = 0, 1r_{\text{norm}}, \ldots, r_{\max}$). In one electrode the channels of all particles are summed up ($Y_{(l)}$), illustrated for six different electrodes in Fig. 3b (bar diagram). Therefore an analytical approach is given with Eq. (3) (continuous channel length distribution $l_k = 0, \ldots, r_{\max}$) and the scale factor is set to 1 length unit. Thus, taking the growing filled channel sections into consideration, the increasing amount of inactive channels can be calculated with Eq. (4). This is shown in Fig. 3c (normalized to the total number of channels involved) for six different size distributions. By merging Eqs. (1) and (4) it is possible to calculate the shell resistance, superimposing the effect of depleted channel section extension and the effect of decreasing active channel quantity. For a certain electrode the development of R_{Shell} can be calculated with Eq. (5) and is exemplarily shown in Fig. 3d assuming different ranges of particle sizes, but having the same amount of active material V_0.

$$g_{(l)} = \frac{\pi r_{\text{particle}}}{A_{\text{channel}}} r_{\text{norm}} = \text{const.} \tag{2}$$

$$Y_{(l)} = \frac{\pi}{2A_{\text{channel}}}\left(\left(\frac{r_{\max}}{r_{\text{norm}}}\right)^2 + \frac{r_{\max}}{r_{\text{norm}}} - \left(\frac{1}{r_{\text{norm}}}\right)^2 + \frac{1}{r_{\text{norm}}}\right) \tag{3}$$

$$M_{(l_k)} = \int_0^{l_k} Y_{(l_k)}\mathrm{d}r = \frac{\pi}{2A_{\text{channel}}}\left(\left(\left(\frac{r_{\max}}{r_{\text{norm}}}\right)^2 + \frac{r_{\max}}{r_{\text{norm}}}\right)\frac{l_k}{r_{\text{norm}}} - \left(\frac{l_k}{3r_{\text{norm}}}\right)^3 + \left(\frac{l_k}{2r_{\text{norm}}}\right)^2\right) \tag{4}$$

$$R_{\text{Shell}(l_k)} = \frac{1}{(M_{(r_{\max})} - M_{(l_k)})2(3V_0)/(\pi r_{\max}^4)}\frac{l_k}{k} \tag{5}$$

From the latter diagram it is cognizable that electrodes containing small particles and particles with a small size distribution have a low shell resistance over a wide SOC range. Hence, they show better DC power performances than electrodes having bigger and wider distributed particles. For short-timed pulses only the electrodes surface is important.

4. Measurements, results and discussion

4.1. The investigated cells and the used test equipment

Investigations according to the two-phase transition behaviour are carried out by measuring Li-ion prototype power cells (A123 Systems) comprising iron containing olivine based cathodes and graphite based anodes. These cells comprise a nominal voltage of 3.3 V. The measurements are made with a Scienlab six channel test bench supplying currents up to ±300 A in a voltage range of −60 to 60 V. During testing the cells are located in a CTS climate chamber (−40 to 90 °C). Cycle tests are made at room temperature (constant 25 °C). Voltage measurements have been carried out with the 24 bit analogue-digital-converters (accuracy: 0.25% of the measured value ± 1 mV) of the test bench. Current measuring was made with LEM hall sensors (0.25% measured value ± 30 mA in a range of −30 to 30 A and 0.25% of the measured value ± 600 mA for higher currents, respectively) integrated to the test bench.

4.2. Differences between charging and discharging of a olivine–graphite–Li-ion cells

To obtain a comprehensive set of charge and discharge curves the cells were loaded with different charge rates and discharge rates (C≙capacity rate A^{-1}). In Fig. 4 plots of complete charge and complete discharge cycles are given. The curves of the cells voltages are plotted versus SOC (SOC is defined to be 100% in the fully charged state and 0% in the discharged state, according to the cells nominal capacity).

It can be seen that the differences among the curves differ between charge and discharge currents (e.g. between 3 C and 6 C charge curve and between 3 C and 6 C discharge curve see Fig. 5). The metallic contacts resistances not having directionality, the active material resistance has to depend on the direction of the load current.

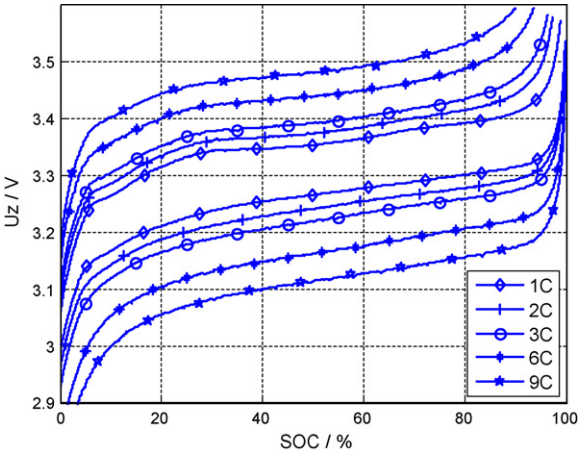

Fig. 4. Curves of the cell voltage during complete cycles with the voltage plotted vs. SOC.

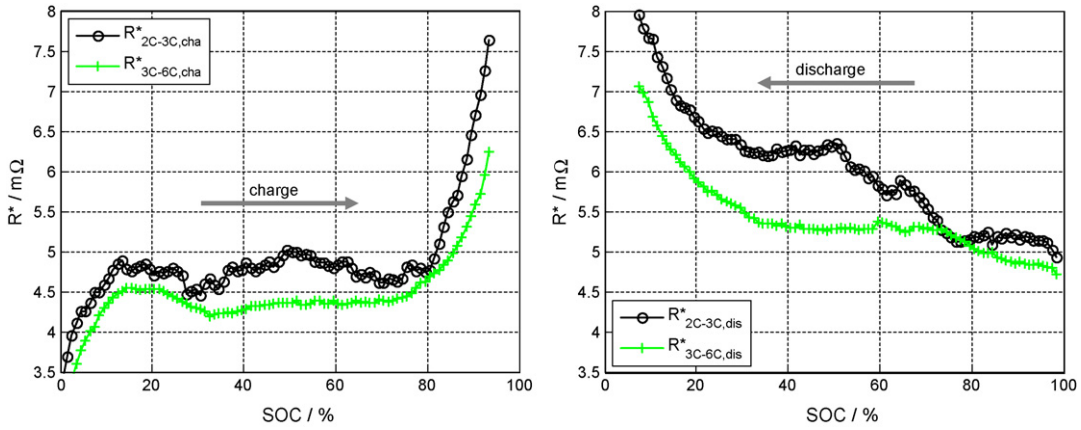

Fig. 5. Illustration of R^* during 2 C, 3 C and 6 C charge (left) and discharge (right), respectively.

This asymmetric behaviour can be elucidated with the shell development within the particles as mentioned above. The path of the charge carriers differs between charge processes and discharge processes in cases of two-phase transition (i.e. in olivine particles). During charge the lithium migrates within the Li-poor regions from the core to the particles surface. During discharge Li migrates within the Li-rich regions from the surface to the phase interface. The Li-rich regions and the Li-poor regions have different properties regarding their Li conductivity. Morgan et al. report an activation barrier for Li hopping of 200 meV of the Li-poor phase and 270 meV of the Li-rich phase of Li_XFePO_4 [19]. The activation barrier influences the mobility and consequently influences the conductivity [20] (→ impact on factor k in Eqs. (1) and (5)). Thus, the Li-poor phase is a better lithium conductor than the Li-rich phase. This is in close agreement with the measured curves.

The development of the cells internal resistance is in further interest. With the difference between two distinct voltage curves the resistance R^* can be identified (calculated with Eq. (6)). OCV is not influencing R^* because only the voltage difference between the curves and the currents are considered.

$$R^*_{I1-I2(SOC)} = \frac{U_{I1(SOC)} - U_{I2(SOC)}}{I1 - I2} \tag{6}$$

Fig. 5 shows R^* for two pairs of load curves (charging current on the left and discharge on the right with 3 C and 6 C, respectively; at higher currents self-heating effects become dominant). In both cases R^* is minimal right after starting the current flow. After that the R^* slightly rises. Finally the gradient drastically increases.

The characteristic of the R^* in a range of 10–90% SOC, given in Fig. 5, is in close agreement with the development of R_{Shell} given in Fig. 3d (neglecting the constant part of R^*, related to the ohmic voltage drops), further indicating the development of distinct shell regions. The current direction dependency of the internal resistance is clearly noticeable, again (differences of approximately 1 mΩ for the illustrated cases).

A further trait of the investigated cells is the special relationship between load current and the cell resistance, also noticeable in Fig. 5. With increasing currents the resistance decreases during charge as well as during discharge. This effect can be related to the Butler–Vollmer equation and is documented elsewhere in more detail (e.g. [21]).

4.3. Path dependent charge and discharge behaviour

4.3.1. Charge history dependency due to the shell phase region development

The current direction dependence of the cells impedances is due to the formation of distinct phase regions within particles of olivine based electrodes as mentioned in Section 4.2. A further evidence for the shell region development and thus the shrinking core theory is done by performing certain partial charge cycles and discharge cycles in order to test charge history dependencies. Special load cycles have been performed to generate particular phase sequences within the particles. In this manner the cells are adjusted to specific SOCs in different ways. At first SOC = 20% was adjusted by discharging a complete charged cell (constant current 3 C; load procedure 1). The other time a complete discharged cell was charged to SOC = 60% and after that discharged to SOC = 20% (procedure 2). The two procedures differ in the direction the current mainly flew

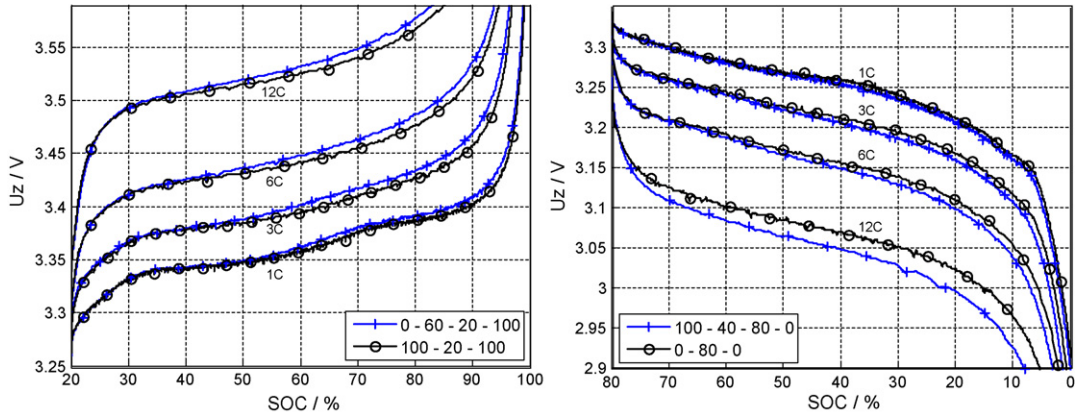

Fig. 6. Differences in the cell voltages according to the load history at different currents (left: charge; right: discharge).

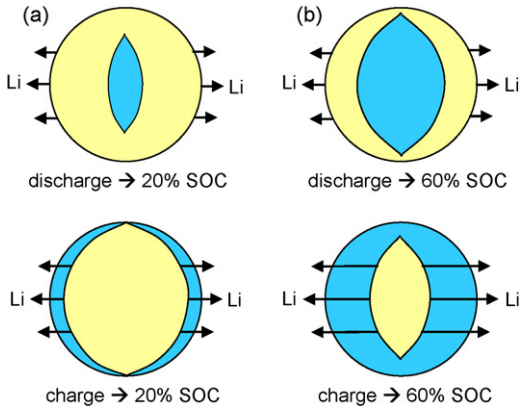

Fig. 7. Comparison of the maximum differences in the phase regions thickness according to the load sequence, illustrated for 20% SOC (a) and 60% SOC (b) in both cases the volume ratio of Li-rich and Li-poor phases are equal.

to reach SOC = 20%. In procedure 1 discharge current is dominant. In procedure 2 charge current sections are dominant. After 30 min rest both times the cells were charged with currents of 1 C till the charging cutoff voltage of 3.6 V was reached. These final charging sections were repeated with different currents (3 C, 6 C, 12 C) right past renewed SOC adjustment (procedures 1 and 2). The cell voltages during the final charge section are depicted on the left hand side of Fig. 6. The voltages are plotted versus SOC. In the legend the sequence of the SOC is given.

The voltages always vary in the same way, according to the load procedures taking part. The voltages after discharge dominated SOC adjustments (procedure 1) are always less than the voltages after charge (procedure 2).

In a second test SOC = 80% was adjusted first by a charge current dominated load regime (0% → 80% SOC; procedure 3) and second SOC = 80% was reached through the discharge dominated procedure 4 (100% → 40% → 80%). Procedures 3 and 4 were performed with 3 C currents. After 30 min rest the cells were discharged to 2 V cutoff voltage. The final discharge section took part with varying currents. The voltages are illustrated on the right hand side of Fig. 6. The voltages after charge current predominating procedure 3 are higher than the voltages after procedure 4, being discharge dominated.

Procedures 1 and 2 end with discharge sections and procedures 3 and 4 end with charge sections, just before reaching the SOC target. Thus, the influence of hysteresis effects or polarisations of the electrodes is minimized. Moreover, the voltages at the beginning of the final load sections are equal. Hence, the different voltages are caused by changing resistances according to the currents applied long time ago. The charge resistance after procedure 1 is less than the one after procedure 2. Furthermore, the discharge resistance after procedure 3 is less compared to procedure 4. Thus, these changing resistances are related to the sequence of the phase regions developed inside the cathodes particles. In the case of procedure 1 an outer Li-rich phase region develops within the Li depleted particles. During the final charge section the Li is directly extracted from the outer shell, passing only short distances inside the active material. In case of procedure 2 a Li-poor shell surrounds the Li-rich core (0% → 60% SOC). After that an additional thin Li-rich shell forms (60% → 20% SOC). First the lithium moves from the outermost shell to the surface during the final charge. After that the Li has to move the whole way from the Li-rich core to the surface. The difference of the distances the Li atoms have to pass determines

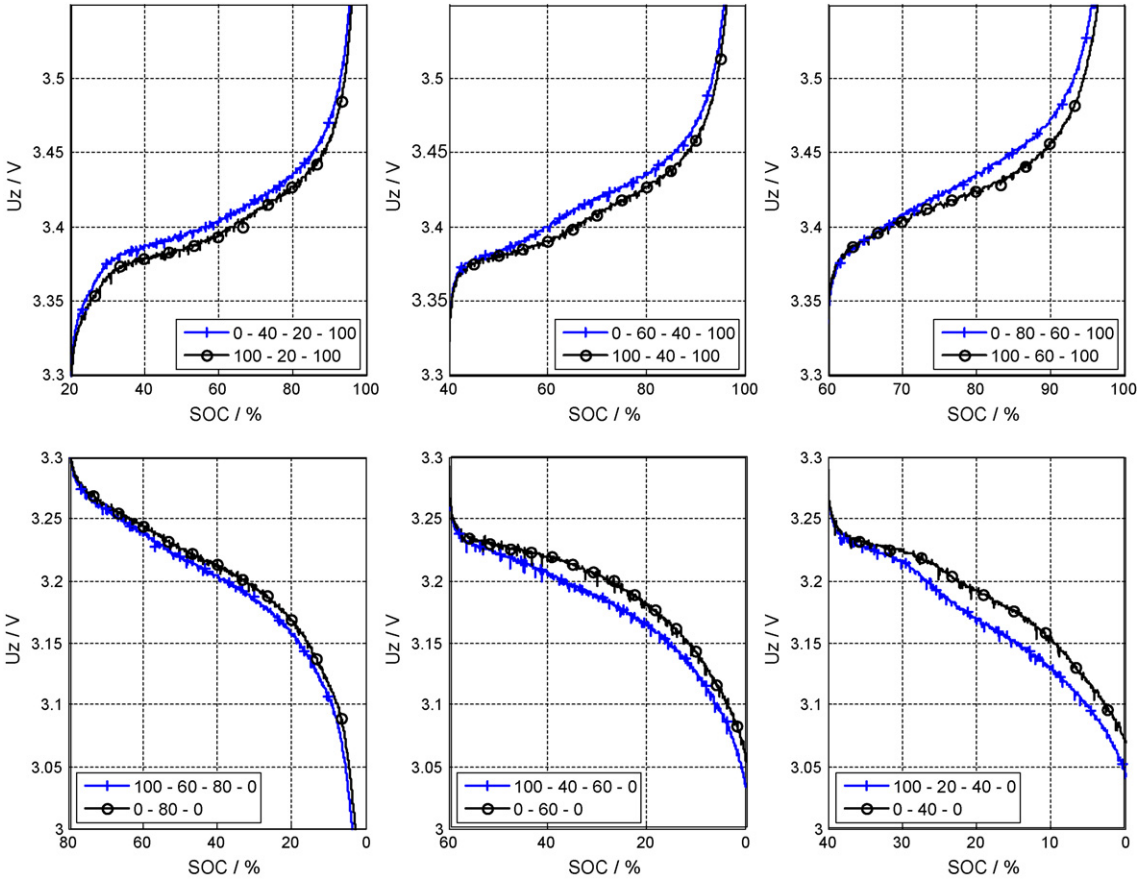

Fig. 8. Measured voltage differences according to the maximum differences in the shell resistance during charge (3 C, top) and discharge (3 C, bottom).

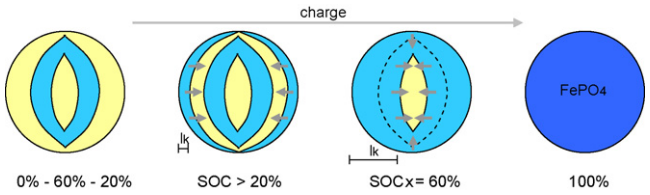

Fig. 9. Illustration of the phase sequence during the vanishing phase effect is taking place.

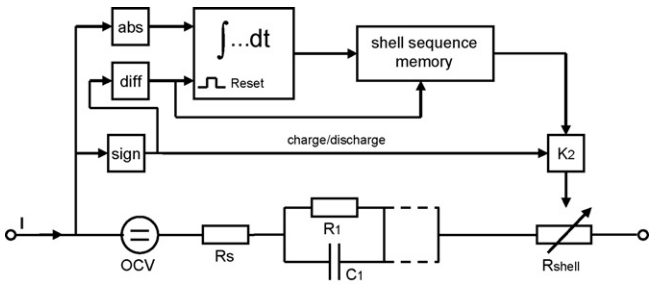

Fig. 11. Cell equivalent electrical circuit considering the phase sequences within the electrodes particles.

the resistance (analogue to Eq. (1) with differing l_k). For procedures 3 and 4 the behaviour is quite equal. After procedure 3 the Li is embedded near the surface during the final discharge. After procedure 4 took place, the Li has to move through the Li-rich shell region to get to the Li-poor core. Thus, the Li atoms have different distances to pass while discharge.

The more the distances inside the particles differ the more the resistances have to vary, although having the same SOC. This matter is schematically illustrated in Fig. 7a and b for two different SOCs, adjusted in different ways. Different length discrepancies can be created by performing various load sequences. Thus, further tests have been made firstly adjusting a SOC through charge and the secondly through discharge with varying charge amounts applied to or extracted from the cells. These charge amounts determine the thickness of the outermost shell. As the charge amounts ascend the differences in the cells resistance increase. This is depicted in Fig. 8 for the charge process as well as for the discharge process.

With increasing SOC the maximum difference in charge resistance increases. Decreasing SOC causes increased maximum differences in the discharge resistances. These differences can gain >20% of the total internal resistance (at room temperature).

4.3.2. *Vanishing phase effect*

In addition to the current direction and the thickness of the outermost phase shell, a further scope is on the characteristics of olivine particles with more complex phase sequences.

Toward the particle centres Li-rich and Li-poor areas may alternate arbitrarily depending on the load profile applied. Every alternation in the current direction causes the formation of a new outermost phase region growing toward the centre. The thickness of the shell underneath shrinks. This process continues until this second shell is completely transformed. When the outermost shell conjoins with the former third shell they become the new outermost shell. This new shell grows further on. This process continues until the next subjacent shell region vanishes and so on. This is illustrated for charge process in Fig. 9.

The disappearance of the second shell increases the distance l_k the Li has to pass suddenly. The amount the distance increases depends on the thickness of the older third shell. Additionally the fraction of active channels decreases rapidly. These two matters cause a sudden rise of the shell resistance (according to Eq. (1)). This matter of fact is measurable during cycling the investigated olivine based Li-ion cells (effect of the vanishing phase). The increasing resistances are visible in the plotted voltages in Fig. 10 (during charge on the left; during discharge on the right). The resistances do not jump for sudden. They gradually increase during a 10–15% SOC change. The increase ends as the SOC of the last current alternation is reached. The earlier growth of the shell resistance is due to the distribution of the migration channel lengths. The shorter migration channels are completely cycled, although during small charge exchanges applied to a cell. In these channels only a part of the phase region sequence can be found. Thus, these channels do not contribute to the occurring vanishing phase effect.

Using the knowledge about the effects caused by the shell phase development and thus the arising influence on the charge and discharge behaviour of the investigated cells, it is possible to evaluate a cell equivalent electric circuit taking these effects in consideration. This cell equivalent circuit is depicted in Fig. 11 implying the assumption only to have migration channels with just one certain length. The involved components Rs, R1, C1, etc. are state of the art in battery modelling (e.g. Randles equivalent circuit). The OCV source supplies the electrode potential of the active compounds involved. These components model the steady state cell voltage and the ohmic and transient overvoltages. Additionally a second part is introduced taking the shell resistance in account. With the current integrator the growth of the outermost shell thickness is considered. If the current direction changes, the actual shell thickness is stored in the shell sequence memory (memory

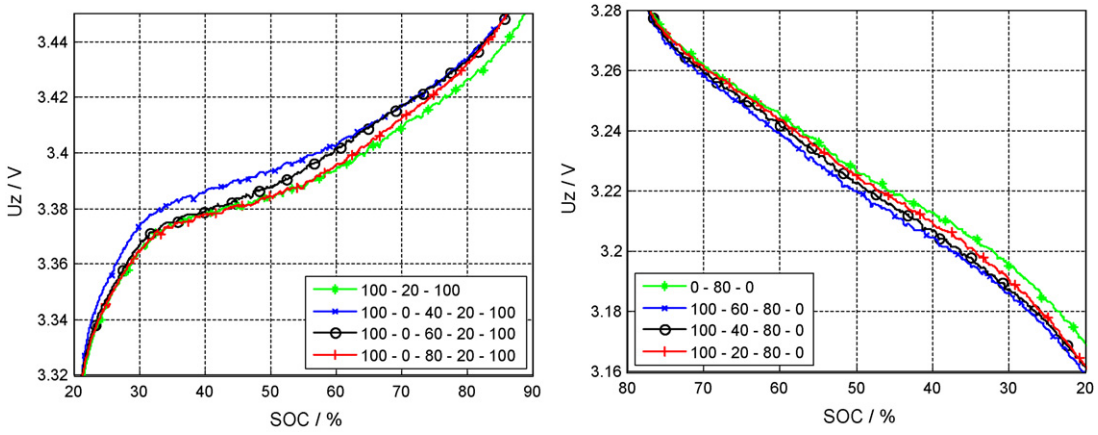

Fig. 10. Voltage responses influenced by the vanishing phase effect (left: charge; right: discharge).

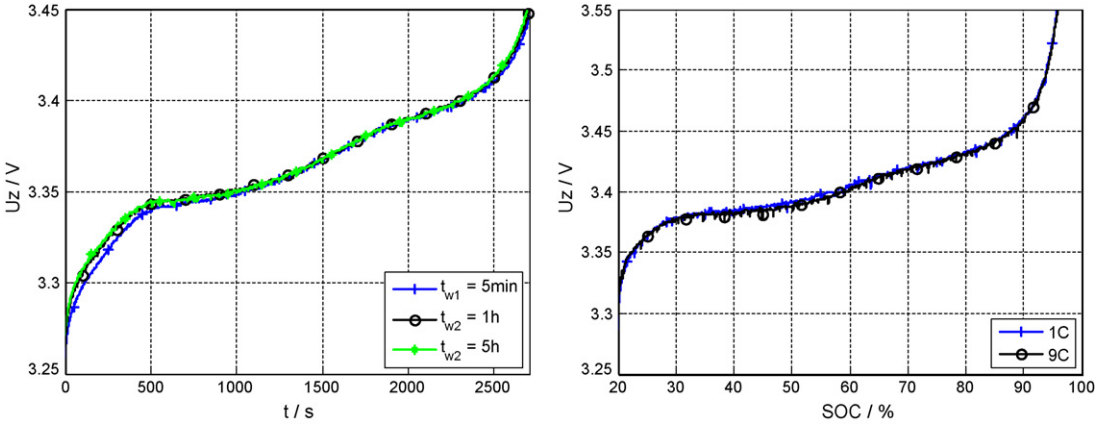

Fig. 12. Comparison of voltage responses to 1 C charge after load procedure 2 with different rest periods (left); Comparison of voltage responses to 1 C charge after procedure 1 performed with different currents.

stack) and the integrator is reset. The information about the shell thickness is used to calculate the shell resistance, with the cell specific factor K_2 also considering the current direction and particles geometry (→ Eqs. (1) and (5), respectively). When the actual shell thickness exceeds the former outermost shell thickness, the actual and the stored third shell information are added. This results in the new outermost shell thickness which is served to the model.

4.3.3. Verification measurements

Finally, measurements are made to test the stability and the durability of the phase sequences within the particles. These measurements are made to make sure that the effects demonstrated above are not caused by (I) the duration of the rest periods, (II) the current during SOC adjustment, (III) the temperature or (IV) any kind of hysteresis effects in OCV.

(I) To check the influence of the rest periods load procedure 2 (0% → 60% → 20% SOC) has been performed for three times. Each time with a different rest period (5 min, 1 h, 5 h) right before the charge section starts. The cell voltages during charge (1 C) are given in Fig. 12 on the left. The voltages are nearly identical. In the first few seconds the voltage after 5 min rest is slightly less due to the not finished voltage recovery after discharge. Thus the phase region separation is permanent and does not disappear after a few of hours.

(II) In order to measure the influence of the load current during SOC adjustment to the phase region development, load procedure 1 (100% → 20%) was run with currents of 1 C and 9 C. The cell voltages during the subsequent charge period (1 C) are shown on the right in Fig. 12. There is no significant difference between the curves. Thus, it can be assumed that the adjustment currents do not impact the effects illustrated in the previous chapters.

(III) Procedures 1 and 2 were carried out and the cells were cooled down to $\vartheta = -10\,^{\circ}C$. After that currents of 1 C were applied. The voltages during the final section are plotted in Fig. 13 (left: charge; right: discharge). The differences between the curves are more significant than the ones between the curves measured during room temperature tests. This is in close agreement with data from the literature reporting the cathode material to have a poor conductivity at low temperatures [5]. The quite unexpected partial decrease of the voltage differences may be caused by internal warming due to the generated power loss. Further investigations to this behaviour are essential, but have not been done yet.

(IV) In a last test the cells were charged to SOC = 20%, adjusted with load procedure 1 and 2. After that a constant charge current (3 C) was applied. At 70% SOC the current flow was interrupted. The voltages decays are given on the left of Fig. 14.

Differences between the curves during current feed (t = 500–1100 s) completely disappear after a few minutes rest. The results for an interrupted discharge are given on the right of Fig. 14 also (procedure 3 and 4 → 3 C discharge to 30% SOC). Again, the voltage differences during load quickly disappear. Both of these tests give evidence that different voltage responses result from varying resistance only, not from varying OCV. Thus, it is proved that new phase region

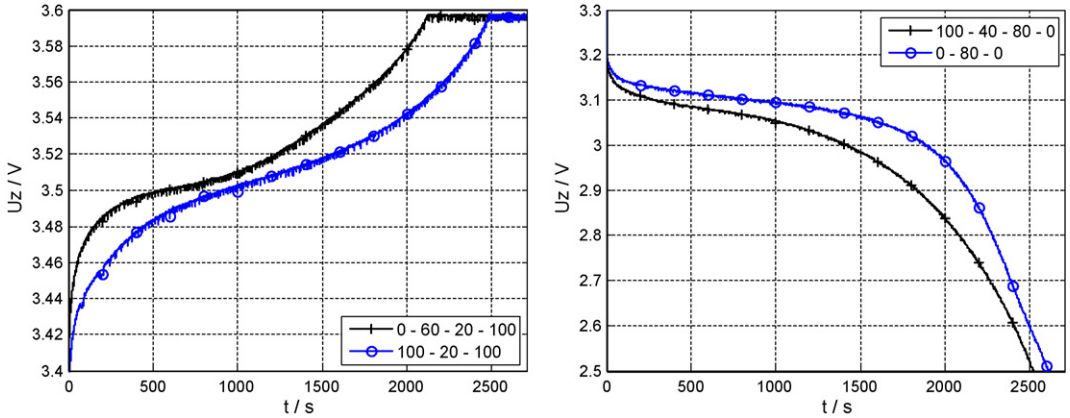

Fig. 13. Typical cells voltages during charge (left) process and discharge (right) process (1 C each) at $\vartheta = -10\,^{\circ}C$ with load procedure 1 and procedure 2, respectively.

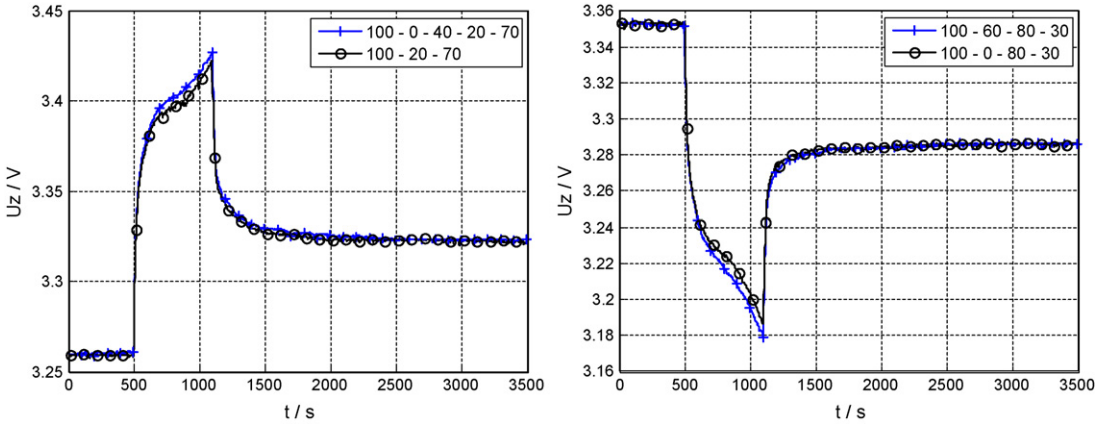

Fig. 14. Interrupted charge (left) and discharge (right) with procedures 1 and 2, respectively 3 and 4.

develops at the particles surface and extends to the centre. Thus, the electrodes electric potential is correlated to the outermost phase region being Li-rich or Li-poor.

5. Conclusion

$LiFePO_4$ has the special trait to perform a two-phase transition during Li intercalation and Li extraction over a wide range of SOC. This matter of fact influences the OCV characteristics as well as the impedance of Li-ion cells containing those cathodes. For the investigated cells (iron containing olivine cathode, graphite anode) it was found that the internal resistance is lower for charge currents than for discharge currents. Therefore an analytical approach is given taking the 1D movement of the Li ions within the particles, the particle shape and the particle size distribution into consideration. Furthermore the two-phase transition causes a long-term dependence between the internal resistance and the load history. The internal resistance can vary more than 20% according to the load sequence. Certain phase sequences within the particles also lead to increased gradients in the internal resistances during load sections (vanishing phase effect). Therefore an electric equivalent circuit was introduced, taking the particles shell development in consideration. Subsequently, the impact of rest period durations, adjustment currents, temperatures and hysteresis on the effects mentioned above were investigated. Only the temperature was identified to influence these effects. At lower temperatures the influences of the shell development on the internal resistance becomes more and more important.

References

[1] J.B. Goodenough, A.K. Padhi, K.S. Nanjundaswamy, C. Masquelier, U.S. Patent No. 5,910,382 (1999).
[2] A.K. Padhi, K.S. Nanjundaswamy, J.B. Goodenough, J. Electrochem. Soc. 144 (1997) 1188–1194.
[3] M. Thackeray, Nat. Mater. 1 (2002) 81–82.
[4] A. Yamada, S.C. Chung, K. Hinokuma, J. Electrochem. Soc. 148 (2001) 224–229.
[5] M. Takahashi, S. Tobishima, K. Takei, Y. Sakurai, J. Power Sources 97–98 (2001) 508–511.
[6] Y.-H. Huang, J.-R. Ying, J.B. Goodenough, Electrochem. Soc. 702 (2007) 110.
[7] K. Striebel, J. Shim, V. Srinivasan, J. Newman, J. Comparison of $LiFePO_4$ from different sources, Lawrence Berkley National Laboratory – Paper LBNL55781, 2004.
[8] M. Gaberscek, et al., J. Power Sources 174 (2007) 944–948.
[9] P.P. Prossini, M. Lisi, D. Zane, M. Pasquali, Solid State Ionics 148 (2002) 45–51.
[10] V.R. Subramanian, H.J. Ploehn, R.E. White, J. Electrochem. Soc. 147 (2000) 2868–2873.
[11] M.D. Levi, D. Aurbach, Electrochim. Acta 45 (1999) 167–185.
[12] N. Meethong, H.-Y. Shadow Huang, S.A. Speakman, W.C. Carter, Y.-M. Chiang, Adv. Funct. Mater. 17 (2007) 1115–1123.
[13] M.D. Levi, K. Gamolsky, D. Aurbach, U. Heider, R. Oesten, J. Electroanal. Chem. 477 (1999) 32–40.
[14] N. Meethong, H.-Y. Shadow Huang, W.C. Carter, Y.-M. Chiang, Electrochem. Solid-State Lett. 10 (2007) 134–138.
[15] M.D. Levi, D. Aurbach, International Conference on Mathematical Modeling and Computer Simulation of Metal Technologies, Ariel, Israel, 2000, pp. 232–243.
[16] V. Srinivasan, J. Newman, J. Electrochem. Soc. 151 (2004) 1517–1529.
[17] K. Thomas-Alyea, 214th Meeting of the Electrochemical Society, 2008 (Abstract #2685).
[18] G. Ceder, G.K. Singh, M.Z. Bazant, arXiv:070.1858v1, 2007 [cond-mat.mtrl-sci].
[19] D. Morgan, A. Van der Ven, C. Ceder, Electrochem. Solid-State Lett. 7 (2004) 30–32.
[20] V. Srinivasan, J. Newman, Electrochem. Solid-State Lett. 9 (2006) 110–114.
[21] G.A. Tsirlina, M.D. Levi, O.A. Perii, D. Aurbach, Electrochim. Acta 46 (2001) 4141–4149.